

## Cryo-EM analysis of the effect of seeding with brain-derived A $\beta$ amyloid fibrils

Peter Benedikt Pfeiffer, Marijana Ugrina, Nadine Schwierz, Christina J. Sigurdson, Matthias Schmidt, Marcus Fändrich

### Angaben zur Veröffentlichung / Publication details:

Pfeiffer, Peter Benedikt, Marijana Ugrina, Nadine Schwierz, Christina J. Sigurdson, Matthias Schmidt, and Marcus Fändrich. 2024. "Cryo-EM analysis of the effect of seeding with brain-derived A $\beta$  amyloid fibrils." *Journal of Molecular Biology* 436 (4): 168422. <https://doi.org/10.1016/j.jmb.2023.168422>.



# Cryo-EM Analysis of the Effect of Seeding with Brain-derived A $\beta$ Amyloid Fibrils

Peter Benedikt Pfeiffer<sup>1,\*</sup>, Marijana Ugrina<sup>2</sup>, Nadine Schwierz<sup>2</sup>,  
Christina J. Sigurdson<sup>3</sup>, Matthias Schmidt<sup>1</sup> and Marcus Fändrich<sup>1</sup>

**1** - Institute of Protein Biochemistry, Ulm University, Helmholtzstraße 8/1, 89081 Ulm, Germany

**2** - Institute of Physics, University of Augsburg, Universitätsstraße 1, 86159 Augsburg, Germany

**3** - Department of Pathology, University of California, San Diego, 9500 Gilman Drive, La Jolla, CA 92093-0612, USA

Correspondence to Peter Benedikt Pfeiffer: [peter.pfeiffer@uni-ulm.de](mailto:peter.pfeiffer@uni-ulm.de) (P.B. Pfeiffer)

<https://doi.org/10.1016/j.jmb.2023.168422>

Edited by Daniel Otzen

## Abstract

A $\beta$  amyloid fibrils from Alzheimer's brain tissue are polymorphic and structurally different from typical in vitro formed A $\beta$  fibrils. Here, we show that brain-derived (ex vivo) fibril structures can be proliferated by seeding in vitro. The proliferation reaction is only efficient for one of the three abundant ex vivo A $\beta$  fibril morphologies, which consists of two peptide stacks, while the inefficiently proliferated fibril morphologies contain four or six peptide stacks. In addition to the seeded fibril structures, we find that de novo nucleated fibril structures can emerge in seeded samples if the seeding reaction is continued over multiple generations. These data imply a competition between de novo nucleation and seed extension and suggest further that seeding favours the outgrowth of fibril morphologies that contain fewer peptide stacks.

© 2024 The Authors. Published by Elsevier Ltd. This is an open access article under the CC BY license (<http://creativecommons.org/licenses/by/4.0/>).

## Introduction

The formation and deposition of amyloid fibrils inside the human body defines a group of diseases that ranges from systemic amyloidosis to different types of neurodegenerative diseases.<sup>1,2</sup> Amyloid fibrils consist of one or several stacks of polypeptide chains that are sometimes referred to as the fibril protofilaments.<sup>3,4</sup> Each stack is held together by intermolecular  $\beta$ -sheet hydrogen bonds (and other interactions) in the direction of the main fibril axis.<sup>5</sup> Amyloid fibrils form by nucleated polymerisation, in which the initial (slow) formation of fibril nuclei represents the rate-limiting step, which is followed by the fast, subsequent outgrowth of fibrils from the nuclei.<sup>6,7</sup> Consistent with this mechanism, it was found that addition of preformed fibrils to solutions of the monomeric fibril precursor protein potently accelerates the fibril formation process.<sup>6,7</sup> Seeding is usually thought to lead to a prion-like

replication of the seed structure in the daughter fibrils. As such, it may underlie the spreading of amyloid pathology inside the body<sup>8</sup> and the transfer of the amyloid pathology across animals if a recipient animal is injected with amyloid-containing tissue extracts from a diseased donor.<sup>9,10</sup>

To confirm the idea of a structural proliferation during seeding, it is important to demonstrate that the structural specifics of the fibrils in the seeded reaction are the same as in the seeds and different from unseeded reactions. In this study we have performed such an analysis in case of A $\beta$ (1–40) peptide. This peptide forms vascular deposits of amyloid fibrils in Alzheimer's disease (AD) and other medical conditions.<sup>11</sup> A $\beta$ (1–40) amyloid fibrils that were purified from AD brain tissue are right-hand twisted and contain three relatively abundant fibril morphologies, termed Morphologies I–III.<sup>12</sup> The three fibril morphologies contain essentially the same peptide conformation but differ in the

number of peptide stacks. Morphology I is composed of two peptide stacks, while there are four stacks in Morphology II and six in Morphology III. In all three morphologies, the peptide conformation was found to be different from previously reported A $\beta$  peptide conformations that were formed *in vitro*.<sup>12</sup>

Using cryo-electron microscopy (cryo-EM) and other methods we investigated whether the structural specifics of these brain-derived A $\beta$  amyloid fibrils can be replicated *in vitro* by seeding a solution of recombinantly expressed A $\beta$ (1–40) peptide with samples of *ex vivo* fibrils. Although this possibility was suggested previously,<sup>13–15</sup> a direct and quantitative side-by-side comparison is missing so far. We find that seeding leads to the selective amplification of only one of the right-hand twisted fibril morphologies (Morphology I) that can be isolated from brain tissue, while the other abundant *ex vivo* fibril morphologies are almost absent in the daughter fibrils. Furthermore, if seeding is continued over several generations, we find that left-hand twisted (*de novo* nucleated) fibril structures can emerge, indicating a competition between seed extension and *de novo* nucleation in the seeded samples.

## Results

### Polymorphism of unseeded A $\beta$ (1–40) fibrils

As a first step to analyse the effect of seeding, we investigated the influence of the solution conditions of the fibril morphology. To that end, we incubated recombinant A $\beta$ (1–40) peptide in 100 mM phosphate buffer, pH 7.4. We find that this treatment results in the formation of large quantities of elongated amyloid fibrils. Two dominant fibril morphologies can be discerned by cryo-EM that are termed here unseeded i and unseeded ii (Supplementary Figure 1a). The two morphologies differ in their cross-over distances ( $108 \pm 8$  nm in unseeded i versus  $80 \pm 4$  nm in unseeded ii,  $n = 30$ ), while their widths are indistinguishable within error (Supplementary Figure 1b). Together, the two morphologies account for 72% of the fibrils in the analysed sample. The remaining 28% of fibrils are morphologically heterogeneous and could not be analysed in further detail (Supplementary Figure 1c). Platinum side shadowing and TEM demonstrated that the fibrils are left-hand twisted (Figure 1a). No right-hand twisted fibrils were found. These properties differ starkly from the known characteristics of *ex vivo* A $\beta$ (1–40) amyloid fibrils from AD brain tissue, which are right-hand twisted, as shown here for the fibrils from two patients (AD1 and AD2, Supplementary Figure 2). We conclude that the fibrils formed *in vitro* do not match the structures of the fibrils that can be extracted from the patient tissue.

### Seeding with *ex vivo* fibrils induces right-hand twisted A $\beta$ (1–40) fibrils

Under our *in vitro* conditions of fibril formation, we find that the lag time of fibril formation is  $12.3 \pm 3.0$  h in the absence of externally added seeds, as demonstrated with time-resolved measurements with the amyloid-binding dye thioflavin T (ThT) (Supplementary Figure 3a). Addition of 0.5% and 1% (w/w) *ex vivo* A $\beta$ (1–40) amyloid fibrils from either patient AD1 or AD2 as seeds at the beginning of the reaction potentially accelerates the reaction and eliminated the lag phase of the reaction (Supplementary Figure 3a). The elimination of the lag phase upon addition of 1% (w/w) seeds was recently found to indicate a templated fibril formation rather than surface catalysis at the lateral side of the seed fibril.<sup>16</sup> Analysis of platinum side shadowed samples of the daughter fibrils obtained after seeding reveals mostly right-hand twisted fibrils, while no left-hand twisted fibrils could be observed, if A $\beta$ (1–40) peptide was seeded with 5% *ex vivo* fibrils (Figure 1b). Lower concentrations of seeds (1 or 0.5%) lead to increased proportions of left-hand twisted fibrils in the daughter generation (Supplementary Figure 3). These data show that seeding has strong effects on the handedness of the fibrils and changes the fibril chirality from a mainly left-hand to a mainly right-hand twisted sample. Consistent observations were made in this regard with the *ex vivo* amyloid fibrils from both patients (Figure 2, Supplementary Figure 3).

Continuing the seeding experiment over multiple generations shows that the percentage of right-hand twisted fibrils is at least 67% in the first two generations, while left-hand twisted amyloid fibrils could not be observed (Figure 2). In the third generation, however, we noted the presence of significant quantities of left-hand twisted fibril structures that now account for  $\sim 7\%$  of the fibrils seen in our sample (Figure 2), while the percentage of right-hand twisted fibrils is decreased to approximately 55%. Consistent observations in this regard were made in both sample series; that is, irrespective of whether the samples were initially seeded with *ex vivo* fibrils from patient AD1 or AD2 (Figure 2).

### Cryo-EM structures of seeded and unseeded A $\beta$ (1–40) amyloid fibrils

To resolve the structures of the fibrils, present in these samples, we used cryo-EM. Reconstruction of the two major fibril morphologies from the unseeded reaction resulted in three-dimensional (3D) maps with spatial resolutions of 2.73 and 2.59 Å (Supplementary Table 1), based on the 0.143 Fourier Shell Correlation (FSC) criterion (Supplementary Figure 4). Molecular models of the fibrils were built based on the 3D maps. Morphology i is C2 symmetrical, while morphology

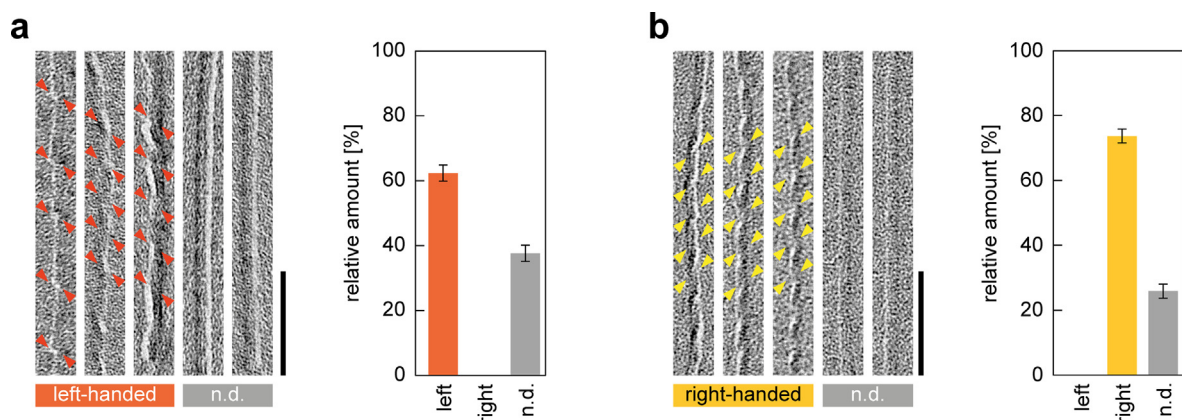


**Figure 1. Handedness of seeded and unseeded A $\beta$ (1–40) fibrils.** (a) TEM images of unseeded A $\beta$ (1–40) amyloid fibrils after platinum side shadowing (left) and a quantification of the sample (right,  $n = 3$  technical replicates with 100 fibrils each). (b) TEM images of seeded (AD2) fibrils after platinum side shadowing (left) and a quantification of the sample (right,  $n = 3$  technical replicates with 100 fibrils each). Arrow heads were drawn to guide the eye. N.d.: handedness could not be determined. Scale bar: 100 nm. The data are representative for the fibrils on 77 (a) and 76 (b) micrographs. Error bars refer to the standard deviation.

ii shows pseudo  $2_1$ -screw symmetry (Figure 3a). Both fibrils were reconstructed with a left-hand twist and differ starkly from the fibrils in the seeded sample, which is dominated by a fibril morphology that shows a width of  $7.6 \pm 0.3$  nm and cross-over distance of  $38.0 \pm 3$  nm ( $n = 30$  each, Supplementary Figure 5a, b). This fibril morphology accounts for 81% of the visible fibrils (Supplementary Figure 5c) and its 3D map could be refined to 2.97 Å (Supplementary Figure 4, Supplementary Table 2). The fibril was reconstructed with a right-hand fibril twist and a pseudo  $2_1$ -screw symmetry (Figure 3a). Its global parameters, 3D map and molecular model correspond to one of the previously described ex vivo fibril morphologies from A $\beta$  peptide (Supplementary Figure 6). There are small changes in the C-terminal half of the peptide model of the two fibrils, although the 3D maps are relatively similar. It is possible that the differences in the models arise from an uncertainty in the fitting of the previous 3D map which has an overall resolution of 4.4 Å, which is lower than the present one (2.97 Å). All fibrils reported here are polar and consist of two peptide stacks.

#### Fold of the fibril proteins in the seeded and unseeded fibrils

The two unseeded fibrils contain similar and relatively extended peptide conformations with ordered structure at residues His13 to Val40 (Figure 3b). The N-terminal parts of the peptide molecules are conformationally disordered and not seen in the 3D maps (Figure 3b). The two fibrils differ in these properties to the seeded fibril, where stable conformation is found between residues Asp1 and Gly37 (Figure 3b). Both fibrils are decorated by regions of relatively diffuse

density (Figure 3b) that show a zig-zag structure in the cross-section and a  $\sim 4.7$  Å regularity in the direction of the fibril z-axis (Supplementary Figure 7). These features imply that the density regions arise from peripherally attached A $\beta$ (1–40) peptides. No such additional density features are seen in the seeded fibril.

The cross- $\beta$  sheets are uniformly formed by parallel strand-strand interactions in the direction of the backbone hydrogen bonds (Figure 4a). The fibrils differ in the number and exact positions of the  $\beta$ -strands within the peptide sequence (Figure 4b). In the seeded fibril, 55% of the residues participate in the formation of the fibril cross- $\beta$  sheets, while only 35% of the residues adopt this type of secondary structure in the unseeded fibrils (Figure 4c). The seeded fibril also shows a higher percentage of residues in the fibril core ( $\sim 93\%$  compared with 70% in the two unseeded fibrils, Figure 4d) and a much larger z-axial extension of each fibril protein (Supplementary Figure 8a). The extension is 8.4 Å in the seeded fibril and 5.3 Å and 4.1 Å in the two unseeded fibrils. These differences enable each peptide molecule of the seeded fibril to interact with eight other peptide molecules, while each peptide molecule of the unseeded fibrils interacts with seven (i) or four (ii) other molecules in the fibril core (Supplementary Figure 8b). Taken together, these features imply that seeded fibrils are more stable than the unseeded fibrils.

#### Seeded fibrils are more stable than unseeded A $\beta$ (1–40) fibrils

To further test this idea, we performed PDBePISA calculations of the strength of the intermolecular interactions. These interactions may occur in the x/y-plane, where they refer to the strength of

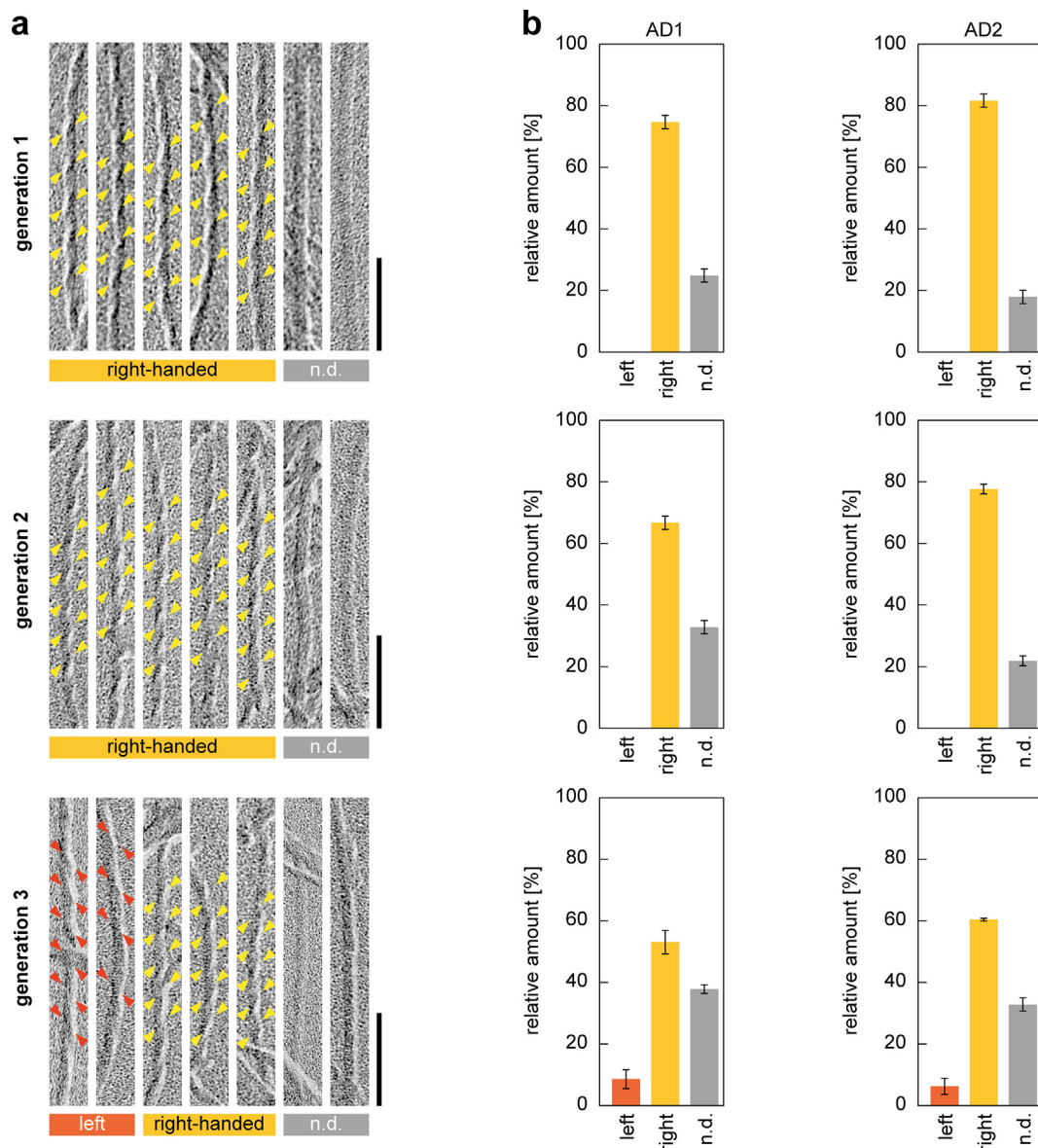


**Figure 2. Fibril handedness in three generations of seeded fibrils.** (a) TEM images of platinum side shadowed fibrils obtained upon seeding with ex vivo  $A\beta(1-40)$  fibrils from patient AD2. Seeding was carried out over three generations. Arrow heads were drawn to guide the eye. N.d.: handedness could not be determined. Scale bar: 100 nm. The data are representative for the fibrils on 20 micrographs collected per sample. (b) Relative amounts of left-hand or right-hand twisted fibrils and of fibrils where the twist could not be determined ( $n = 3$  technical replicates with 100 fibrils each) upon seeding with fibrils from patients AD1 (left) and AD2 (right) prior to generation 1. Error bars refer to the standard deviation. Top row: first generation; middle row: second generation; bottom row: third generation.

interactions between the two peptide stacks, or in the direction of the fibril z-axis, where they relate to the interactions between the adjacent molecular layers of the fibril. Analysis of the two unseeded fibrils with PDBePISA yields Gibbs free energies of dissociation ( $\Delta G_{\text{diss}}$ ) of 12.5 kcal/mol for the dissociation of a peptide from the other peptide stack (x/y interactions, [Supplementary Figure 9](#)). While this value is higher than the one obtained for the seeded fibril (8 kcal/mol), the z-axial interactions are stronger in the seeded than in the

unseeded fibrils. The  $\Delta G_{\text{diss}}$  values to separate the adjacent molecular layers in the direction of the z-axis is 35 kcal/mol in the seeded fibril and only 20 kcal/mol (i) and 29 kcal/mol (ii) in the two unseeded fibrils. That is, each molecular layer of the seeded fibril is stabilised by 43 kcal/mol, while unseeded fibrils are stabilised by 33 kcal/mol (i) and 41 kcal/mol (ii), respectively ([Supplementary Figure 9c](#)).

We then performed molecular dynamics (MD) simulations for 200 ns in explicit water. Analysis of

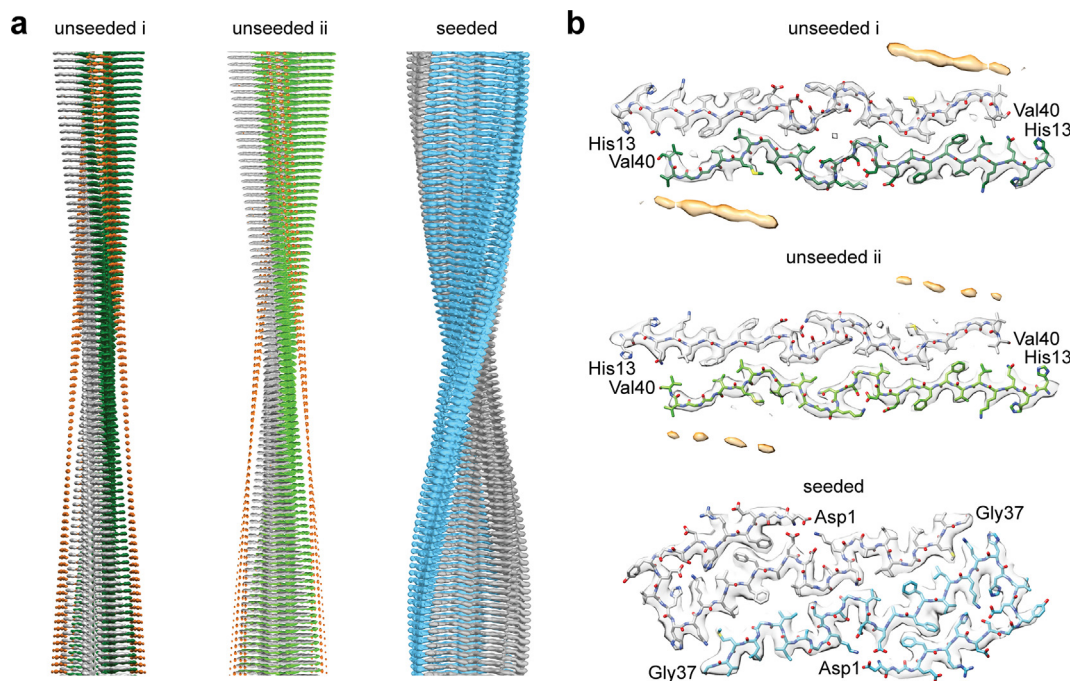


**Figure 3. Cryo-EM reconstruction of seeded and unseeded fibrils.** (a) Side view of the 3D maps of the two unseeded fibrils and the seeded fibril. (b) Cross-sectional views of one molecular layer of the 3D maps (grey), overlaid with the molecular models. Ochre: Poorly resolved density features in the 3D maps of the unseeded fibrils that could not be assigned to the peptides in the fibril core. The first and last residue of the fibril core are indicated.

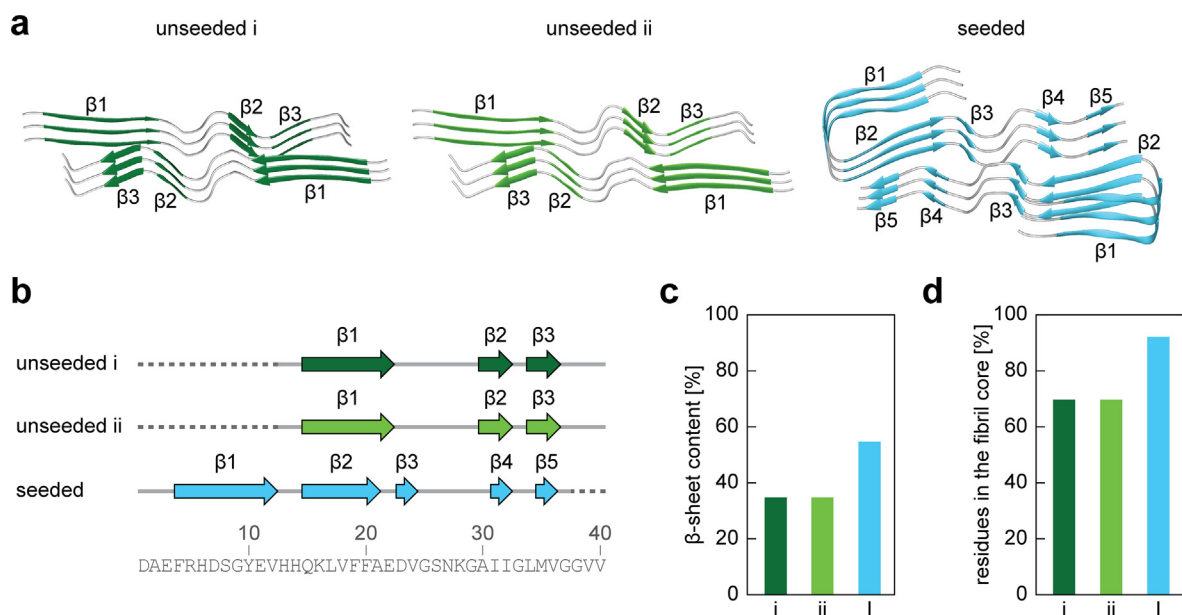


**Figure 4.  $\beta$ -sheet structure of seeded and unseeded fibrils.** (a) Ribbon diagrams of 3-layer stacks of the three fibrils. (b) Sequence of the A $\beta$ (1–40) peptide showing the location of the  $\beta$ -sheets (arrows). Structurally disordered regions are indicated as dotted lines. (c) Number of residues arranged in a  $\beta$ -sheet structure (dark green: unseeded i; light green: unseeded ii; blue: seeded I). (d) Percentage of residues in the fibril core.

the seeded fibril at three different temperatures (300 K, 350 K and 400 K) shows that the fibril remains stable and that the peptides at the fibril tips do not dissociate over the course of the

simulation (Supplementary Figure 10a). Both unseeded fibril structures are less stable and deviate more substantially from the experimentally determined starting structure, as indicated by the

higher root mean square deviation (RMSD) (Supplementary Figure 10b). Interestingly, the stability of the seeded fibril is strongly affected by the protonation state, and thus the charge of the three histidine residues (His6, His13 and His14). The conformational stability of the peptides of the seeded fibril is significantly higher if the histidine residues are simulated without charges, whereas no such charge effect is seen for the two unseeded fibrils (Supplementary Figure 10b). These data demonstrate the high stability of the seeded fibril and its dependence on the folding of the peptide N-terminus and the protonation state of its three histidine residues.

Finally, we examined the stability of the two fibril samples to proteinase K. Both samples are relatively resistant to proteolysis under the chosen set of conditions, but we find significantly more proteolysis in the unseeded fibril samples compared with the seeded ones, as evidenced by a p-value of 0.001 for samples digested for 30 or 60 min (Supplementary Figure 11). As a result, approximately 85% of the seeded fibrils are able to withstand proteolytic digestion for 60 min, while only ~60% of the unseeded fibrils resist proteolysis in our experiment. All analyses of the samples reported here show consistently that the seeded fibrils are more stable than the unseeded fibrils.

## Discussion

In this study we demonstrate that A $\beta$ (1–40) amyloid fibrils, which were purified from the meningeal tissue of two AD patients, are able to seed solutions of the freshly dissolved, recombinant A $\beta$ (1–40) peptide (Supplementary Figure 3) and proliferate the seed structure to the fibrils in generation 1 (Supplementary Figure 6). This proliferation is only efficient for one of the fibril morphologies of the seeds (Morphology I) (Supplementary Figure 6), while the other two abundant ex vivo fibril structures (Morphologies II and III)<sup>12</sup> are almost absent in the seeded sample. Morphology I constitutes 28% of the fibrils that can be isolated from brain tissue<sup>12</sup> and 81% of the seeded fibrils (Supplementary Figure 5). Morphologies II and III constitute 34% and 15% of the fibrils in the seeds<sup>12</sup> but only 2% and 5% of the fibrils in the seeded sample (Supplementary Figure 5). These data demonstrate that seeding does not replicate all fibril structures with equal efficiency, but that there is a preferential proliferation of a specific fibril morphology.

This fibril morphology contains two peptide stacks, while the inefficiently proliferated fibril Morphologies II and III contain four or six peptide stacks, respectively.<sup>12</sup> This preferential proliferation of the thinnest fibril morphology during seeding corresponds to the results of a recent seeding study with fibrils from murine systemic AA amyloidosis.

These fibrils consist of serum amyloid A (SAA) protein and they occur in two main fibril morphologies<sup>17</sup>: one containing two and one containing three fibril protein stacks.<sup>18</sup> Upon seeding, however, only the two-stack fibril morphology was found to be proliferated, while the three-stack fibril morphology was essentially absent after seeding.<sup>19</sup> Furthermore, there is long-standing evidence that the de novo fibril nucleation is faster for thin fibril morphologies (protofibrils) compared with thicker ones (mature fibrils).<sup>20,21</sup> Taken together, we suggest that there is a kinetic preference of fibril structures with a smaller number of peptide stacks.

Another important finding made by our study is that ex vivo fibril structures are not stable over multiple generations and that left-hand twisted fibril morphologies emerge in generation 3 (Figure 2). This observation was made irrespective of whether the samples were seeded with fibrils from patient AD1 or AD2 (Figure 2). As left-hand twisted amyloid fibrils are characteristic for de novo nucleated, in vitro formed A $\beta$ (1–40) fibrils (Figure 1) and absent in brain-derived ex vivo A $\beta$ (1–40) fibrils (Supplementary Figure 2), we conclude that their appearance is indicative of a competition between de novo nucleation and seed extension in our samples (Figure 5). Seed extension proliferates the structure of the seeds, while de novo nucleation leads to fibril structures that are determined by the conditions of fibril formation, incubation time and stochastic factors.<sup>3,22</sup> In our case, we find that the solution conditions lead to left-hand twisted fibril morphologies (Figure 1). That such fibril structures emerge at higher generations of the seeded sample series implies that seed extension is not efficient enough to prevent all de novo nucleation reactions.

Two explanations may be offered why this lack of efficiency becomes apparent at later generations. First, de novo nucleation may lead to only a small proportion of fibrils in each generation. However, these fibrils will also be able to act as seeds in the subsequent generations such that the de novo nucleated fibril morphologies may progressively accumulate in the sample and become abundant in later generations. Second, it is possible that the proliferation of the ex vivo fibril structure requires a molecular cofactor that is present in the ex vivo fibril sample after its isolation from the brain but becomes diluted from generation to generation. Therefore, proliferation of the ex vivo fibril structure will eventually lose in efficiency and de novo nucleation will become increased.

Our study relates to a series of previous publications which aimed to reproduce ex vivo fibril structures from tau,  $\alpha$ -synuclein, A $\beta$  or SAA protein under controlled conditions inside a test tube.<sup>13,14,19,23</sup> Although high resolution structural data were not always reported, some studies described an in vitro replication of the ex vivo fibril structures,<sup>19,24–26</sup> while others noted structural

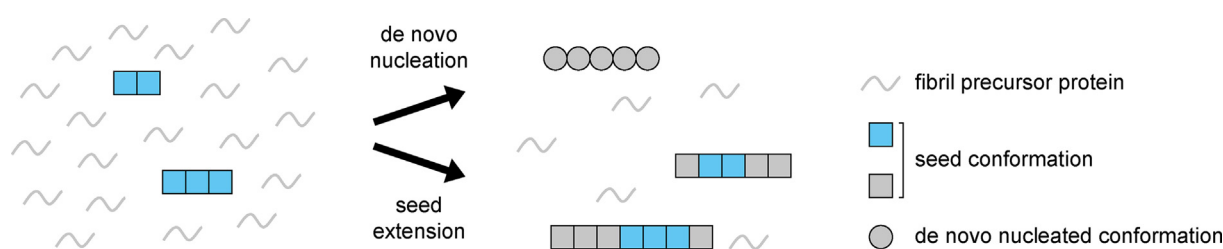


**Figure 5. Competition between seed extension and de novo fibril nucleation.** Schematic representation of the competition between seed extension and de novo fibril nucleation. Left: solution of monomeric fibril precursor protein containing seeds (dark grey). Right: Generation 1 can contain de novo nucleated fibrils (top) and fibrils arising from seed extension (bottom).

deviations of the daughter filaments compared with the seeds.<sup>23</sup> In case of a study in which recombinant SAA protein was seeded with ex vivo AA amyloid fibrils,<sup>19</sup> a small number of in vitro-like (de novo nucleated) fibril morphologies were observed upon seeding, along with fibrils that reflect the structure of the seeds. Furthermore, several previous studies report fibril structures in higher generation samples of A $\beta$ (1–40) fibrils that were initially seeded with ex vivo fibrils or crude brain extracts<sup>13–15</sup> that correspond to the fibril morphologies which we find here in the unseeded fibril samples (Supplementary Figure 12). As these fibril morphologies are, as we show here, from de novo nucleation and as these and other left-hand twisted fibrils are essentially absent in the ex vivo fibrils (Supplementary Figure 2) and in the first two generations of the seeded samples (Figure 2), we conclude that they arose from de novo nucleation rather than seed extension.

The present data are ultimately evidence for the view that pathogenic ex vivo amyloid fibrils are structurally different from and more stable than (unseeded) in vitro fibrils. In our case we find that the ex vivo-like seeded fibril possesses a higher  $\beta$ -sheet content than unseeded in vitro fibrils and contains more residues in the fibril core (Figure 4). Each peptide molecule interacts also with more peptides from the fibril core than in the unseeded fibrils (Supplementary Figure 8). Taken together with the data obtained with our PDBePISA calculations (Supplementary Figure 9), MD simulations (Supplementary Figure 10) and proteinase K digestion (Supplementary Figure 11), the ex vivo-like seeded fibril is more stable than the unseeded fibrils. Hence, our current data are further support to the concept that the high stability of disease-associated amyloid fibril morphologies, in particular to proteolysis, is a key feature determining the pathogenic relevance of protein aggregates as it enables the accumulation of specific fibril morphologies inside the body.<sup>27,28</sup>

In case of A $\beta$ (1–40) fibrils, we find that the stability of the ex vivo-like, seeded fibril structure depends on the charge state of the three histidine residues (Supplementary Figure 10b). The protonation state of histidine depends on the microenvironment around this residue that is

defined by the folding of the polypeptide chain as well as by the physico-chemical environment. Hence, the formation of the observed fibrils may involve environmental conditions that lead to a deprotonation of the histidine residues inside the body, such as a neutral-basic pH environment, or the interaction with one or several anionic chemical components, which compensate the charge at the histidine residues. Although no such cofactor could be identified in our 3D map, we noted that our map contains regions of diffuse density that may originate from bound molecular components. These compounds may not present the high helical symmetry of the fibril core and become averaged out during reconstruction. One candidate for this cofactor is an anionic glycosaminoglycan, as glycosaminoglycans are known for decades to bind to A $\beta$  and other amyloid fibrils,<sup>29</sup> to accelerate fibril formation<sup>30</sup> and to modify the fibril morphology.<sup>31</sup> While further research is required to further test this hypothesis and to establish the molecular nature of this cofactor, if existing. Once identified, however, it could be used to characterize its binding to the fibril structure through additional MD experiments.

## Methods

### Recombinant protein expression and purification

Human A $\beta$ (1–40) peptide was recombinantly expressed in *Escherichia coli* RV308 as described previously.<sup>32</sup> In brief, cells were transformed with a pMAL-c2x vector (New England Biolabs) containing the A $\beta$ (1–40) coding region that is N-terminally fused to His-tagged maltose binding protein (MBP) and a tobacco etch virus (TEV) cleavage site. Protein purification consisted of five steps: (i) chromatographic separation with nickel-sepharose fast flow resin (Cytiva), (ii) chromatographic separation with Q sepharose fast flow resin (Cytiva), (iii) cleavage of the MBP-A $\beta$  fusion protein with TEV protease into MBP and A $\beta$ (1–40), (iv) chromatographic separation with nickel-sepharose fast flow resin (Cytiva), (v) chromatographic separation with source 15 RPC reversed phase medium (GE

Healthcare). Purified A $\beta$ (1–40) was lyophilised and kept frozen until usage.

### Fibril extraction from tissue

Ex vivo A $\beta$  fibrils were extracted from 50 mg human meningeal tissue from two patients (AD1 and AD2) which were described previously.<sup>12</sup> The extraction was performed according to a modified version of a previously described protocol.<sup>33</sup> Briefly, 50 mg meningeal tissue was chopped into small pieces using a scalpel and homogenised in 500  $\mu$ l tris(hydroxymethyl)aminomethane (Tris) calcium buffer A (20 mM Tris, 138 mM NaCl, 2 mM CaCl<sub>2</sub>, 0.1% (w/v) NaN<sub>3</sub>, pH 8.0) using a pellet pestle. The tissue pieces were washed eight times in Tris calcium buffer A, followed by a centrifugation step at 3,100  $\times$  g for 5 min at 4 °C. The resulting pellet was resuspended in 1 ml protease inhibitor solution (one tablet ethylenediaminetetraacetic acid (EDTA)-free protease inhibitor cocktail (cOmplete™, Roche) in 7 ml Tris calcium buffer A) and subjected to overnight digestion with 5 mg/ml collagenase from *Clostridium histolyticum* (Sigma) at 37 °C and 300 rpm. Afterwards, the homogenate was centrifuged at 3,100  $\times$  g for 30 min at 4 °C and washed three times with 500  $\mu$ l Tris EDTA buffer (20 mM Tris, 140 mM NaCl, 10 mM EDTA, 0.1% (w/v) NaN<sub>3</sub>, pH 8.0), followed by centrifugation at 3,100  $\times$  g for 5 min at 4 °C. The resulting pellet was resuspended in 100  $\mu$ l ice-cold water and centrifuged at 3,100  $\times$  g for 5 min at 4 °C. The supernatant containing amyloid fibrils (fibril extract) was carefully removed and stored at 4 °C. The extraction steps with water were repeated for another five times, generating six fibril extracts in total. The analysis was conducted based on the permission of the Ethics Committee of Ulm University (210/13). The material was collected following the legal requirements in the U.S.A. for collecting human tissue samples.

### In vitro fibrillation and seeding of A $\beta$ (1–40)

Unseeded amyloid fibrils were generated by incubating 0.1 mg/ml recombinant A $\beta$ (1–40) protein in 100 mM phosphate buffer, pH 7.4, at 37 °C for 72 h. Seeded amyloid fibrils were generated at the same incubation conditions, but the solutions contained 5% (w/w) of ex vivo fibrils. For the data shown in Figure 2 fresh solutions of A $\beta$ (1–40) were seeded with 5% (w/w) peptide from the previous generation. The fibrillation reactions were carried out in Protein LoBind tubes (Eppendorf) with a sample volume of 100  $\mu$ l.

### Platinum side shadowing

A sample volume of 3.5  $\mu$ l from the seeded and unseeded fibrils was applied to glow-discharged formvar and carbon coated grids (200 mesh, Electron Microscopy Sciences). The grids were

incubated for 1 min at room temperature and blotted with filter paper. Afterwards the grids were washed with water three times. A layer of  $\sim$ 1 nm platinum was applied on the grids at an angle of 40°. The grids were analysed at 120 kV on a JEM-1400 transmission electron microscope (Jeol).

### Cryo-electron microscopy

A sample volume of 3.5  $\mu$ l from the seeded and unseeded fibrils was applied to glow-discharged holey carbon coated grids (400 mesh C-flat 1.2/1.3, Protochips). The grids were blotted with filter paper and plunge frozen in liquid ethane using an automatic plunge freezer EM GP2 (Leica). Grids were initially screened at 200 kV using a JEM-2100 transmission electron microscope (Jeol). The data sets for reconstruction were recorded at 300 kV with a Titan Krios transmission electron microscope (Thermo Fisher Scientific). A K2 summit camera (Gatan) was used to obtain the images of the seeded fibrils, while a Falcon 4i camera (Thermo Fisher Scientific) was used for the unseeded fibril sample. The specific data acquisition parameters are listed in Supplementary Tables 1 and 2.

### Helical reconstruction

The obtained movie frames of the seeded fibrils were gain corrected with IMOD<sup>34</sup> and motion corrected and dose weighted with MotionCor2.<sup>35</sup> The images of the unseeded fibrils were gain corrected with RELION 3.1.3.<sup>36</sup> and motion corrected with MotionCor2.<sup>35</sup> In both cases, the contrast transfer function (CTF) of the motion corrected images was estimated using CTFFIND-4.1.<sup>37</sup> The following helical reconstruction was performed using RELION 3.1.3.<sup>36</sup>

In case of the unseeded fibrils, images of fibril morphologies i and ii were manually picked on the micrographs and extracted with a box size of 300 and 240 pixels respectively. A reference-free two-dimensional (2D) classification was performed over 40 rounds for morphology i with a regularisation parameter  $T = 2$ . Afterwards, 2D classes with  $\sim$ 4.7 Å spacing were selected. An initial 3D map was reconstructed, using a featureless cylinder which was created with the relion\_helix\_toolbox. The reconstructed 3D map showed a C2 symmetry and was used as a reference for 3D classification. A high-resolution refinement was performed, using the best 3D class as a reference. The resulting 3D map was further improved by CTF refinement and Bayesian polishing. The final 3D map was masked by a soft edge mask and post processed.

In case of the unseeded morphology ii, 2D classification was performed with a regularisation parameter of  $T = 2$  for the first 25 rounds and with  $T = 4$  for additional 15 rounds. 2D classes with a clear  $\sim$ 4.7 Å spacing were selected to generate

an initial 3D map based on a featureless cylinder as a reference. The resulting pseudo  $2_1$ -screw symmetrical 3D map was used as a reference for 3D classification. Using the best 3D class as a reference, a high-resolution refinement was performed. The obtained 3D map was further improved by Bayesian polishing and CTF-refinement. The final 3D map was masked and post processed.

In case of the seeded fibril morphology I, segments were extracted with a box size of 200 pixels. A reference-free 2D classification was performed over 25 rounds with a regularisation parameter  $T = 2$ . 2D classes with a clearly separated  $\sim 4.7$  Å spacing were selected for the creation of an initial 3D map, using a featureless cylinder as a reference. The resulting 3D map showed a pseudo  $2_1$ -screw symmetry and was used as a reference for 3D classification. Using the best 3D class as a reference, a high-resolution refinement was performed. The final 3D map was masked and post processed.

### Model building

The structure of the seeded fibril was built using the ex vivo fibril Morphology I (Protein Data Bank (PDB): 6SHS<sup>12</sup> as a reference. The structure of the unseeded morphologies i and ii were created de novo. All structures were built using Coot<sup>38</sup> and structural refinement was performed with phenix.real\_space\_refine.<sup>39</sup> Restraints imposed during modelling were non-crystallographic symmetry constraints, Ramachandran, rotamer and atomic geometry restraints. Peptide  $\beta$ -sheets were manually assigned and used as structure restraints. Validation was performed with MolProbity,<sup>40</sup> using atomic clashes, rotamer and Ramachandran outliers as well as geometry restraints. The fitting of the reconstructed 3D maps by a structure were first performed on one molecular layer. After obtaining a reasonable fit of the structure to the 3D map, a six-layer stack was created, using the Situs implementation pdsymm.<sup>41</sup> The process of modelling and refinement was repeated until the fit of the structure to the map was satisfactory and the refinement converged. EMRinger scores<sup>42</sup> were calculated for all final structures to demonstrate the excellent fit to the 3D map and the high accuracy of the assigned backbone conformation and side-chain rotamers.

### MD simulations

All-atom MD simulations of the three fibril morphologies (unseeded i, ii and seeded I) were performed. In the simulations, we assumed the histidines to be either protonated or deprotonated. Fibrils with deprotonated histidines were simulated at different temperatures (300 K, 350 K and 400 K). An additional simulation was performed at 300 K with protonated histidines. Each structure was placed in a cubic simulation box with an edge

length of about 136.2 Å. The boxes were filled with water and neutralised with 0.15 M NaCl, leading to system sizes of about 335,752 atoms. The force field parameters for the proteins were taken from the Amber99sb-star-ildn force field<sup>43</sup> and the TIP4P-Ew<sup>44</sup> model was used for water. For NaCl, the Mamatkulov-Schwierz force field parameters were used.<sup>45</sup>

MD simulations were performed using the Gromacs simulation package, versions 2020.6 and 2022.5.<sup>46</sup> The system was simulated at constant number of particles, pressure and temperature. Periodic boundary conditions were applied, and the particle-mesh Ewald method was used for the periodic treatment of Coulombic interactions. Bonds to hydrogen atoms were constrained using the LINCS algorithm and a 2 fs time step was used. To equilibrate the systems, first an energy minimization was performed with the steepest descent algorithm. The systems were equilibrated for 1 ns, first with a constant number of particles, volume and temperature and then at constant pressure. For the production run, 200 ns long simulations were performed, employing the velocity-rescaling thermostat with a stochastic term and a time constant of 0.1 ps and isotropic Parrinello-Rahman pressure coupling with a time constant of 0.5 ps. For each of the production runs, the RMSD was calculated with the respective experimental structure as a reference.

### Accession Numbers

The cryo-EM images were deposited in the Electron Microscopy Public Image Archive with the accession codes **EMPIAR-11595** (unseeded sample) and **EMPIAR-11596** (seeded sample). The reconstructed 3D maps were deposited in the Electron Microscopy Data Bank with the accession codes **EMD-17166** (unseeded morphology i), **EMD-17167** (unseeded morphology ii) and **EMD-17168** (seeded morphology I). The molecular models were deposited in the Protein Data Bank with the accession codes **8OT1** (unseeded morphology i), **8OT3** (unseeded morphology ii) and **8OT4** (seeded morphology I). Other data are available from the corresponding author upon reasonable requests. The amount of fibrils extracted from Alzheimer's brain tissue and the amount of seeded fibrils, used in this study are limited.

### Author contributions

P.B.P. and M.U. carried out experiments. P.B.P., M.U., N.S., M.S. and M.F. analysed the data. C.J.S. provided material and reagents and M.F. designed the research. P.B.P. and M.F. wrote the paper, supported by all other authors.

## DECLARATION OF COMPETING INTEREST

The authors declare that they have no known competing financial interests or personal relationships that could have appeared to influence the work reported in this paper.

## Acknowledgements

This work was funded by a grant from the Deutsche Forschungsgemeinschaft (FA 456/24-1) to M.F. The authors acknowledge technical support by Felix Weis and Simon Fromm (European Molecular Biology Laboratory, Heidelberg) and Paul Walther (Ulm University). We thank Marius Kollmer (Ulm University) for helpful discussions. All cryo-EM data were collected at the European Molecular Biology Laboratory, Heidelberg (Germany). The cryo-EM data collection was funded partly by iNEXT (Horizon 2020, European Union).

## Appendix A. Supplementary data

Supplementary data to this article can be found online at <https://doi.org/10.1016/j.jmb.2023.168422>.

Received 21 September 2023;

Accepted 23 December 2023;

Available online 28 December 2023

### Keywords:

aggregation;  
amyloid beta;  
cryo-electron microscopy;  
prion;  
protein misfolding

### Abbreviations:

2D, two-dimensional; 3D, three-dimensional; AD, Alzheimer's disease; CTF, contrast transfer function; cryo-EM, cryo-electron microscopy; EDTA, ethylenediaminetetraacetic acid; FSC, Fourier Shell Correlation; MBP, maltose binding protein; MD, molecular dynamics; PDB, Protein Data Bank; RMSD, root mean square deviation; SAA, serum amyloid A; TEV, tobacco etch virus; ThT, thioflavin T; TRIS, tris(hydroxymethyl) aminomethane

## References

- Chiti, F., Dobson, C.M., (2017). Protein misfolding, amyloid formation, and human disease: a summary of progress over the last decade. *Annu. Rev. Biochem.* **86**, 27–68.
- Buxbaum, J.N., Dispenzieri, A., Eisenberg, D.S., Fändrich, M., Merlini, G., Saraiva, M.J.M., Sekijima, Y., Westermark, P., (2022). Amyloid nomenclature 2022: update, novel proteins, and recommendations by the International Society of Amyloidosis (ISA) Nomenclature Committee. *Amyloid* **29**, 213–219.
- Fändrich, M., Nyström, S., Nilsson, K.P.R., Böckmann, A., LeVine III, H., Hammarström, P., (2018). Amyloid fibril polymorphism: a challenge for molecular imaging and therapy. *J. Intern. Med.* **283**, 218–237.
- Ke, P.C., Zhou, R., Serpell, L.C., Riek, R., Knowles, T.P.J., Lashuel, H.A., Gazit, E., Hamley, I.W., Davis, T.P., Fändrich, M., Otzen, D.E., Chapman, M.R., Dobson, C.M., Eisenberg, D.S., Mezzenga, R., (2020). Half a century of amyloids: past, present and future. *Chem. Soc. Rev.* **49**, 5473–5509.
- Eisenberg, D.S., Sawaya, M.R., (2017). Structural studies of amyloid proteins at the molecular level. *Annu. Rev. Biochem.* **86**, 69–95.
- Jarrett, J.T., Lansbury, P.T., (1993). Seeding “one-dimensional crystallization” of amyloid: A pathogenic mechanism in Alzheimer's disease and scrapie? *Cell* **73**, 1055–1058.
- Knowles, T.P.J., Vendruscolo, M., Dobson, C.M., (2014). The amyloid state and its association with protein misfolding diseases. *Nature Rev. Mol. Cell Biol.* **15**, 6.
- Jucker, M., Walker, L.C., (2013). Self-propagation of pathogenic protein aggregates in neurodegenerative diseases. *Nature* **501**, 45–51.
- Lundmark, K., Westermark, G.T., Nyström, S., Murphy, C.L., Solomon, A., Westermark, P., (2002). Transmissibility of systemic amyloidosis by a prion-like mechanism. *Proc. Natl. Acad. Sci.* **99**, 6979–6984.
- Jucker, M., Walker, L.C., (2011). Pathogenic protein seeding in Alzheimer disease and other neurodegenerative disorders. *Ann. Neurol.* **70**, 532–540.
- Thal, D.R., Walter, J., Saito, T.C., Fändrich, M., (2015). Neuropathology and biochemistry of A $\beta$  and its aggregates in Alzheimer's disease. *Acta Neuropathol.* **129**, 167–182.
- Kollmer, M., Close, W., Funk, L., Rasmussen, J., Bsoul, A., Schierhorn, A., Schmidt, M., Sigurdson, C.J., Jucker, M., Fändrich, M., (2019). Cryo-EM structure and polymorphism of A $\beta$  amyloid fibrils purified from Alzheimer's brain tissue. *Nature Commun.* **10**, 1.
- Lu, J.-X., Qiang, W., Yau, W.-M., Schwieters, C.D., Meredith, S.C., Tycko, R., (2013). Molecular Structure of  $\beta$ -Amyloid Fibrils in Alzheimer's Disease Brain Tissue. *Cell* **154**, 1257–1268.
- Ghosh, U., Thurber, K.R., Yau, W.-M., Tycko, R., (2021). Molecular structure of a prevalent amyloid- $\beta$  fibril polymorph from Alzheimer's disease brain tissue. *PNAS* **118**, e2023089118.
- Crooks, E.J., Fu, Z., Irizarry, B.A., Zhu, X., Van Nostrand, W.E., Chowdhury, S., Smith, S.O., (2022). An electrostatic cluster guides A $\beta$ 40 fibril formation in cerebral amyloid angiopathy 2022.12.22.521588 [Preprint] *bioRxiv*. <https://doi.org/10.1101/2022.12.22.521588>.
- Koloteva-Levine, N., Aubrey, L.D., Marchante, R., Purton, T.J., Hiscock, J.R., Tuite, M.F., Xue, W.F., (2021). Amyloid particles facilitate surface-catalyzed cross-seeding by acting as promiscuous nanoparticles. *PNAS* **118**, e2104148118.
- Annamalai, K., Liberta, F., Vielberg, M.-T., Close, W., Lilie, H., Gührs, K.-H., Schierhorn, A., Koehler, R., Schmidt, A., Haupt, C., Hegenbart, U., Schönland, S., Schmidt, M., Groll, M., Fändrich, M., (2017). Common fibril structures imply systemically conserved protein misfolding pathways in vivo. *Angew. Chem.* **129**, 7618–7622.

18. Liberta, F., Rennegarbe, M., Rösler, R., Bijzet, J., Wiese, S., Hazenberg, B.P.C., Fändrich, M., (2019). Morphological and primary structural consistency of fibrils from different AA patients (common variant). *Amyloid* **26**, 164–170.
19. Heerde, T., Rennegarbe, M., Biedermann, A., Savran, D., Pfeiffer, P.B., Hitznerberger, M., Baur, J., Puscalau-Girtu, I., Zacharias, M., Schwierz, N., Haupt, C., Schmidt, M., Fändrich, M., (2022). Cryo-EM demonstrates the in vitro proliferation of an ex vivo amyloid fibril morphology by seeding. *Nature Commun.* **13**, 1.
20. Walsh, D.M., Hartley, D.M., Kusumoto, Y., Fezoui, Y., Condron, M.M., Lomakin, A., Benedek, G.B., Selkoe, D.J., Teplow, D.B., (1999). Amyloid  $\beta$ -protein fibrillogenesis: structure and biological activity of protofibrillar intermediates. *J. Biol. Chem.* **274**, 25945–25952.
21. Lashuel, H.A., LaBrenz, S.R., Woo, L., Serpell, L.C., Kelly, J.W., (2000). Protofilaments, filaments, ribbons, and fibrils from peptidomimetic self-assembly: implications for amyloid fibril formation and materials science. *J. Am. Chem. Soc.* **122**, 5262–5277.
22. Wei, G., Su, Z., Reynolds, N.P., Arosio, P., Hamley, I.W., Gazit, E., Mezzenga, R., (2017). Self-assembling peptide and protein amyloids: from structure to tailored function in nanotechnology. *Chem. Soc. Rev.* **46**, 4661–4708.
23. Lövestam, S., Schweighauser, M., Matsubara, T., Murayama, S., Tomita, T., Ando, T., Scheres, S.H., (2021). Seeded assembly in vitro does not replicate the structures of  $\alpha$ -synuclein filaments from multiple system atrophy. *FEBS open bio* **11**, 999–1013.
24. Al-Hilaly, Y.K., Foster, B.E., Biasetti, L., Lutter, L., Pollack, S.J., Rickard, J.E., Serpell, L.C., (2020). Tau (297–391) forms filaments that structurally mimic the core of paired helical filaments in Alzheimer’s disease brain. *FEBS Letter* **594**, 944–950.
25. Lövestam, S., Koh, F.A., van Knippenberg, B., Kotecha, A., Murzin, A.G., Goedert, M., Scheres, S.H., (2022). Assembly of recombinant tau into filaments identical to those of Alzheimer’s disease and chronic traumatic encephalopathy. *Elife* **11**, e76494.
26. Lutter, L., Al-Hilaly, Y.K., Serpell, C.J., Tuite, M.F., Wischik, C.M., Serpell, L.C., Xue, W.F., (2022). Structural identification of individual helical amyloid filaments by integration of cryo-electron microscopy-derived maps in comparative morphometric atomic force microscopy image analysis. *J. Mol. Biol.* **434**, 167466.
27. Bansal, A., Schmidt, M., Rennegarbe, M., Haupt, C., Liberta, F., Stecher, S., Puscalau-Girtu, I., Biedermann, A., Fändrich, M., (2021). AA amyloid fibrils from diseased tissue are structurally different from in vitro formed SAA fibrils. *Nature Commun.* **12**, 1.
28. Schönfelder, J., Pfeiffer, P.B., Pradhan, T., Bijzet, J., Hazenberg, B.P.C., Schönland, S.O., Hegenbart, U., Reif, B., Haupt, C., Fändrich, M., (2021). Protease resistance of ex vivo amyloid fibrils implies the proteolytic selection of disease-associated fibril morphologies. *Amyloid* **28**, 243–251.
29. Ancsin, J.B., (2003). Amyloidogenesis: Historical and modern observations point to heparan sulfate proteoglycans as a major culprit. *Amyloid* **10**, 67–79.
30. Iannuzzi, C., Irace, G., Sirangelo, I., (2015). The effect of glycosaminoglycans (GAGs) on amyloid aggregation and toxicity. *Molecules* **20**, 2.
31. McLaurin, J., Franklin, T., Zhang, X., Deng, J., Fraser, P. E., (1999). Interactions of Alzheimer amyloid- $\beta$  peptides with glycosaminoglycans. *Eur. J. Biochem.* **266**, 1101–1110.
32. Claus, S., Meinhardt, K., Aumüller, T., Puscalau-Girtu, I., Linder, J., Haupt, C., Walther, P., Syrovets, T., Simmet, T., Fändrich, M., (2017). Cellular mechanism of fibril formation from serum amyloid A1 protein. *EMBO Rep.* **18**, 1352–1366.
33. Annamalai, K., Gührs, K.-H., Koehler, R., Schmidt, M., Michel, H., Loos, C., Gaffney, P.M., Sigurdson, C.J., Hegenbart, U., Schönland, S., Fändrich, M., (2016). Polymorphism of amyloid fibrils in vivo. *Angew. Chem. Int. Ed.* **55**, 4822–4825.
34. Kremer, J.R., Mastronarde, D.N., McIntosh, J.R., (1996). Computer visualization of three-dimensional image data using IMOD. *J. Struct. Biol.* **116**, 71–76.
35. Zheng, S.Q., Palovcak, E., Armache, J.-P., Verba, K.A., Cheng, Y., Agard, D.A., (2017). MotionCor2: anisotropic correction of beam-induced motion for improved cryo-electron microscopy. *Nature Methods* **14**, 4.
36. Scheres, S.H.W., (2020). Amyloid structure determination in RELION-3.1. *Acta Crystallogr. Sect. D* **76**, 94–101.
37. Rohou, A., Grigorieff, N., (2015). CTFFIND4: Fast and accurate defocus estimation from electron micrographs. *J. Struct. Biol.* **192**, 216–221.
38. Emsley, P., Lohkamp, B., Scott, W.G., Cowtan, K., (2010). Features and development of Coot. *Acta Crystallogr. Sect. D* **66**, 4.
39. Liebschner, D., Afonine, P.V., Baker, M.L., Bunkóczi, G., Chen, V.B., Croll, T.I., Hintze, B., Hung, L.-W., Jain, S., McCoy, A.J., Moriarty, N.W., Oeffner, R.D., Poon, B.K., Prisant, M.G., Read, R.J., Richardson, J.S., Richardson, D. C., Sammito, M.D., Sobolev, O.V., Adams, P.D., (2019). Macromolecular structure determination using X-rays, neutrons and electrons: recent developments in Phenix. *Acta Crystallogr. Sect. D* **75**, 10.
40. Williams, C.J., Headd, J.J., Moriarty, N.W., Prisant, M.G., Videau, L.L., Deis, L.N., Verma, V., Keedy, D.A., Hintze, B. J., Chen, V.B., Jain, S., Lewis, S.M., Arendall III, W.B., Snoeyink, J., Adams, P.D., Lovell, S.C., Richardson, J.S., Richardson, D.C., (2018). MolProbity: more and better reference data for improved all-atom structure validation. *Protein Sci.* **27**, 293–315.
41. Wriggers, W., (2012). Conventions and workflows for using Situs. *Acta Crystallogr. Sect. D* **68**, 4.
42. Barad, B.A., Echols, N., Wang, R.-Y.-R., Cheng, Y., DiMaio, F., Adams, P.D., Fraser, J.S., (2015). EMRinger: side chain-directed model and map validation for 3D cryo-electron microscopy. *Nature Methods* **12**, 10.
43. Lindorff-Larsen, K., Piana, S., Palmo, K., Maragakis, P., Klepeis, J.L., Dror, R.O., Shaw, D.E., (2010). Improved side-chain torsion potentials for the Amber ff99SB protein force field: improved protein side-chain potentials. *Proteins Struct. Funct. Bioinforma.* **78**, 1950–1958.
44. Horn, H.W., Swope, W.C., Pitner, J.W., Madura, J.D., Dick, T.J., Hura, G.L., Head-Gordon, T., (2004). Development of an improved four-site water model for biomolecular simulations: TIP4P-Ew. *J. Chem. Phys.* **120**, 9665–9678.
45. Mamatkulov, S., Schwierz, N., (2018). Force fields for monovalent and divalent metal cations in TIP3P water based on thermodynamic and kinetic properties. *J. Chem. Phys.* **148**, 074504.
46. Van Der Spoel, D., Lindahl, E., Hess, B., Groenhof, G., Mark, A.E., Berendsen, H.J.C., (2005). GROMACS: Fast, flexible, and free. *J. Comput. Chem.* **26**, 1701–1718.